Adaptive Local Multigrid Methods for the Solution of Time Harmonic Eddy Current Problems

Oliver Sterz*†, Andreas Hauser† and Gabriel Wittum†

*Computer Simulation Technology (CST) GmbH
Bad Nauheimer Str. 19, 64289 Darmstadt, Germany

†Interdisciplinary Center for Scientific Computing (IWR),
University of Heidelberg, 69120 Heidelberg, Germany

***Abstract*— The efficient computation of large eddy current problems with finite elements requires adaptive methods and fast optimal iterative solvers like multigrid methods. This paper provides an overview of the most important implementation aspects of an adaptive multigrid scheme for time-harmonic eddy currents. It is shown how the standard multigrid scheme can be modified to yield an $\mathcal{O}(N)$ complexity even for general adaptive refinement strategies, where the number of unknowns N can grow slowly from one to the next refinement level. Algorithmic details and numerical examples are given.**

I. Introduction

The computational work to solve time harmonic eddy current problems with finite element methods (FEMs) is dominated by the solution of the resulting linear systems of equations. For this reason, fast iterative solving strategies becomes necessary.

One of the currently fastest methods is the multigrid method that operates on a hierarchy of grids. Moreover, this method can be designated as "natural" in some sense, if one thinks of another key feature of an efficient electromagnetic computational software: Adaptivity, which allows the resolution of strongly local effects and enables the automatic generation of adequate meshes. The subsequent application of a posteriori error estimation and local mesh refinement in the adaptive computation will create the very hierarchy of grids a multigrid scheme operates on.

In this paper we will focus on the various algorithmic aspects to realize an efficient adaptive multigrid scheme, yielding a computational software tool for time harmonic eddy current problems.

The outline of the paper is as follows. In the next section, the (variational) eddy current formulation based on the electric field is introduced. In section three, we look at important aspects of the applied edge finite elements and details of the adaptive red-green-refinement scheme, as well as the error estimator and refinement strategy. Section four is devoted to the construction of the local multigrid scheme for time harmonic eddy currents including detailed implementation aspects. Finally, in the last section convergence and robustness of the proposed local multigrid scheme is examined when applied to several time-harmonic eddy currents examples, including a realistic gas insulated switchgear (GIS) with non-trivial geometry.

II. $\mathbf{E}$-Based Eddy Current Formulation

The eddy current model is a magneto-quasistatic approximation of the full Maxwell-equations. It reads

$$\mathbf{curl}\,\mathbf{E} = -\mathrm{i}\omega\,\nu^{-1}\,\mathbf{H} \quad \text{in } \Omega \tag{1}$$

$$\mathbf{curl}\,\mathbf{H} = \mathbf{j}_G + \sigma\,\mathbf{E} \quad \text{in } \Omega\,, \tag{2}$$

where Ω is a three-dimensional bounded domain with exterior normal vector field $\mathbf{n}$ on its boundary Γ. As usual, ω denotes the angular frequency, $\mathbf{E}$ and $\mathbf{H}$ stand for the electric and magnetic field, respectively, and $\mathbf{j}_G$ is the imposed current density (generator current). The material coefficients σ and ν are $L^\infty(\Omega)$-fields and denote the conductivity and the magnetic reluctivity, respectively. We denote the part of the domain where $\sigma > 0$ by Ω_C and its complement by Ω_I, where we assume $\sigma \equiv 0$.

The eddy current model is reasonable if two conditions are met, see [1] for a proof:

1) The frequency is low enough, such that the wavelength is much larger than the spatial region of interest, i.e. $\omega\sqrt{\nu/\epsilon} \ll 1$.
2) The conductivity is high enough, such that no space charges need to be taken into account in the conductive region, i.e. $\omega\epsilon/\sigma \ll 1$.

Equations (1) and (2) have to be supplemented by appropriate boundary conditions on Γ. We assume electric boundary conditions on the part $\Gamma_D \subset \Gamma$ of the boundary,

$$\mathbf{n} \times \mathbf{E} = \mathbf{g}\,, \tag{3}$$

and magnetic boundary conditions on the remaining part Γ_N,

$$\mathbf{n} \times \mathbf{H} = 0\,. \tag{4}$$

Note that the restriction to zero magnetic boundary conditions is only for simplicity, since none of the examples presented later has non-zero magnetic boundary conditions.

There are two dual ways to cast Eq. (1)- (4) into a variational formulation, see e.g. [2]. Here, we chose the "electric" formulation, using Eq. (1) in strong and Eq. (2) in weak form.

Defining the space

$$\boldsymbol{\mathcal{U}}(\mathbf{g}) := \{\mathbf{u} \in \mathbf{H}(\mathbf{curl};\Omega) \,|\, \mathbf{n} \times \mathbf{u} = \mathbf{g} \text{ on } \Gamma_D\}\,,$$

the variational formulation reads: *Find* $\mathbf{E}$ *in* $\boldsymbol{\mathcal{U}}(\mathbf{g})$*, such that*

$$\int_\Omega \nu\, \mathbf{curl}\,\mathbf{E} \cdot \mathbf{curl}\,\mathbf{E}'\, d\mathbf{x} + \mathrm{i}\omega \int_{\Omega_C} \sigma \mathbf{E} \cdot \mathbf{E}'\, d\mathbf{x} = -\mathrm{i}\omega \int_\Omega \mathbf{j}_G \cdot \mathbf{E}'\, d\mathbf{x} \qquad \forall \mathbf{E}' \in \boldsymbol{\mathcal{U}}(0)\,. \quad (5)$$

Note that (5) does not uniquely define $\mathbf{E}$ in whole Ω—an electrostatic component in Ω_I still needs to be fixed. However, since this can easily be done in a post-processing step by solving a Poisson problem in Ω_I, this is not a restriction, see e.g. [3]. Moreover, $\mathbf{curl}\,\mathbf{E}$, and thus the magnetic field $\mathbf{H}$, the currents and the Ohmic losses are uniquely defined, which are of primary interest in the majority of modeling situations.

III. Adaptive Finite Elements

Solutions of time harmonic eddy current problems usually show strongly local phenomena due to the skin effect or edge and corner singularities at material jumps and boundaries. In order

- to minimize the computational resources (time and memory) or
- to compute a solution with maximal accuracy for given computational resources,

it is necessary to construct optimal meshes which resolve these local effects without being extremely fine everywhere in Ω.

These optimal meshes will be automatically constructed with the aid of an a posteriori error estimator, as shown in the algorithm in Fig. 1.

```
procedure Adaptive Computation
{
    repeat
    {
        assemble discretization
        solve system
        estimate error
        if (error < tolerance or no resources available)
        then stop
        adapt mesh
    }
}
```

Fig. 1. Adaptive computation.

In the following we will look at the discretization, error estimation and mesh adaptation in more detail, whereas solving the linear system of equations will be postponed to section IV.

A. Discretization

To discretize problem (5) we rely on $\mathbf{H}(\mathbf{curl};\Omega)$-conformal lowest order edge elements on simplicial meshes $\mathcal{T}_h$, often called Whitney-1-forms, referring to the very structure the edge elements are embedded in—the Whitney complex. One important consequence of this structure is the existence of discrete potentials, which are important e.g. for the construction of appropriate smoothers, see [4].

The simplicial meshes $\mathcal{T}_h$ cover Ω^h—an adequate polyhedral approximation of Ω—and are assumed to be *consistent*, i.e. for two distinct simplices $T \in \mathcal{T}_h$ and $T' \in \mathcal{T}_h$, their intersection $T \cap T'$ is either empty, a node, an edge or a face of $\mathcal{T}_h$. Thus, no hanging nodes exist.

Denoting the edge element function associated to the edge with index i by $\boldsymbol{\xi}_i$ we will end up with the complex symmetric system

$$\boldsymbol{A}\,\mathbf{x} = \mathbf{b}\,,$$

where the matrix and right hand side vector coefficients read

$$A_{ij} = \int_{\Omega^h} \nu\, \mathbf{curl}\,\boldsymbol{\xi}_i \cdot \mathbf{curl}\,\boldsymbol{\xi}_j\, d\mathbf{x} + i\omega \int_{\Omega^h} \sigma\, \boldsymbol{\xi}_i \cdot \boldsymbol{\xi}_j\, d\mathbf{x}$$

$$b_i = -i\omega \int_{\Omega^h_C} \mathbf{j}_G \cdot \boldsymbol{\xi}_i\, d\mathbf{x}\,.$$

The dimension of the system is the number of edges in the mesh. In case the (geometrically approximated) Dirichlet-boundary Γ^h_D is non-empty, the system can be reduced to the "free edges" with non-prescribed voltages as usual.

B. Local Error Estimator

To apply the algorithm in Fig. 1, we use the residual based error-estimator presented in [5].

Let $\mathbf{E}_h$ be the discrete solution. The error estimate has been shown to be reliable and efficient, i.e. for the error $\mathbf{E} - \mathbf{E}_h$ we have

$$c\,\eta \le \|\mathbf{E} - \mathbf{E}_h\| \le C\,\eta\,,$$

with constants c, C. Furthermore, η has a local sum representation,

$$\eta^2 = \sum_{T \in \mathcal{T}_h} \eta_T^2\,, \quad (6)$$

which can be used to indicate the error distribution.

The η_T are computable element-wise with low cost using low order quadrature rules and consists of three parts,

$$\eta_T = \sqrt{(\eta_T^\perp)^2 + (\eta_F^0)^2 + (\eta_F^\perp)^2}\,,$$

which measure the different aspects of the error in Ampère's law, Eq. (2). (Remember that, using an electric formulation, Faraday's law is satisfied pointwise, whereas Ampère's law is satisfied only "mesh-weakly", i.e. for $h \to 0$.)

We list the estimated error components for completeness,

$$(\eta_T^{\perp})^2 = \min\left(\frac{\omega^2}{\nu}\, h_T^2, \frac{\omega}{\sigma}\right) \|\sigma\, \mathbf{E}_h + \mathbf{J}_{G,h}\|^2_{\boldsymbol{L}^2(T)} \ , \tag{7a}$$

$$(\eta_F^{\perp})^2 = \sum_{F\in\mathcal{F}(T)} \frac{h_F\, \omega^2}{2\,\nu_T\,(1+\frac{\nu_F}{\nu_T})^2} \|[\mathbf{n}\times\nu\ \mathbf{curl}\,\mathbf{E}_h]_F\|^2_{\boldsymbol{L}^2(F)} \ , \tag{7b}$$

$$(\eta_F^{0})^2 = \sum_{F\in\mathcal{F}(T)} \frac{h_F\, \omega\, \sigma_T}{2(\sigma_T+\sigma_F)^2} \left\|[\mathbf{n}\cdot(\sigma\, \mathbf{E}_h + \mathbf{J}_{G,h})]_F\right\|^2_{\boldsymbol{L}^2(F)} \ , \tag{7c}$$

where by $[\cdot]_F$ we denote the jump along an element face, $\mathcal{F}(T)$ is the set of faces bounding element T and material coefficients indexed by T and F denote the limit from the element T and from the neighbor element at face F, respectively.

Particularly, since for Whitney-1-forms we have $\mathbf{H} = const.$ element-wise, $\mathbf{curl}\,\mathbf{H}_h = 0$ in every T, $(\eta_T^{\perp})$ measures the deviation from Ampère's law in the interior of the elements. The terms $(\eta_F^{\perp})^2$ and $(\eta_F^{0})^2$ measure the jump of the tangential magnetic field and the normal jump of currents across element faces, respectively, where Ampère's law implies zero jumps in both cases.

C. Mesh Adaptation

1) Selection Strategy: Given the local errors $\{\eta_T\}_{T\in\mathcal{T}_h}$ several strategies exists to decide which elements shall be refined, see e.g. [6]. In this paper, we use a simple maximum strategy, as shown in the algorithm in Fig. 2, where typical values for ξ are $\xi = 0.25$ or $\xi = 0.50$.

procedure SetRefinementMarks($\mathcal{T}_h, \{\eta_T\}_T, \xi \in (0,1)$)
{
  $\eta_{max} \leftarrow \max_{T\in\mathcal{T}_h}(\eta_T)$
  forall $(T \in \mathcal{T}_h)$ **do**
    if $(\eta_T > \xi\,\eta_{max})$ **then** mark T for refinement
}

Fig. 2. Simple selection strategy.

2) Red-Green Refinement: The marked elements will be *regularly* refined, e.g. by the so called "red-rule", where in 2D a triangle is subdivided into for congruent triangles, see [7], and in 3D a tetrahedron is split into 8 son-elements in a special way, see e.g. [8]. These son-elements are associated to three similarity classes.

Consequently, since the number of generated similarity classes stays bounded, the subsequent application of the regular refinement rule will not detoriate the element-quality, i.e. regular refinement is a *stable refinement*.

However, not all elements are usually marked for refinement. Thus, in order to avoid "hanging nodes", so-called "green closure" elements are introduced, which connect the regularly ("red") refined elements. Finally, unrefined elements are copied to the next refinement level, usually called "yellow copy-elements". Remember that, in order to apply the geometrical multigrid techniques presented in the next section, a *hierarchy* of grids $\{\mathcal{T}_l\}_l$, $\mathcal{T}_0 = \mathcal{T}_h$, will be generated, i.e. after refinement, the father elements still exist in memory. An example situation with "red", "green" and "yellow" elements is shown in Fig. 3.

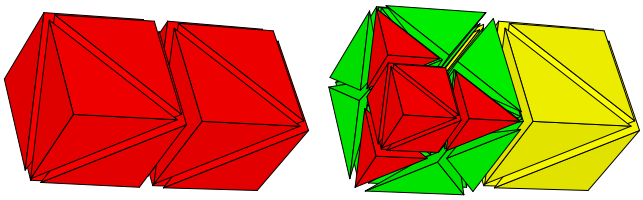

Fig. 3. Two cubes build of tetrahedra grid (left), Red-Green refined grid (right), where the very left tetrahedron has been refined by the red rule. The tetrahedra of the right cube are not refined, they are yellow copy elements. The green closure connects the refined and unrefined elements in a consistent manner.

The green-refinement, however, is not stable, i.e. subsequent application of the described refinement in the following adaptive passes may generate elements with decreasing quality (more and more obtuse angles).

This problem can be solved by

1) the rule "only red elements can be refined"—note that on the initial grid $\mathcal{T}_0$ all elements are red by definition—
2) and by making use of the hierarchical structure.

This means, that the red-green refinement is not a mere map between two grids $\mathcal{T}_l \mapsto \mathcal{T}_{l+1}$, but between two grid-*hierarchies* ("multi-grids") $\{\mathcal{T}_l\}_{0\le l\le L} \mapsto \{\mathcal{T}'_l\}_{l=0\le l\le L'}$, where $\mathcal{T}_0 = \mathcal{T}'_0$, and usually (but not necessarily) $L > L$.

The global red-green refinement used works as follows: First the refinement-marks are restricted to the lower mesh-levels and, if already possible, green closure elements are introduced (top-down-phase). Then, at every level, starting with the lowest level (bottom-up-phase)

- green closure elements are removed if necessary,
- new red elements are inserted,
- new green elements are inserted (closure computation)
- and other elements are copied to the finer level.

By doing so, green elements, that otherwise would be refined again, are replaced by regular refined elements and the resulting global refinement algorithm is stable. For more details, see [8] and [9].

Finally, we note that there are several ways to compute the green closure. One possibility is to use a *complete* rule set, which enables the refinement algorithm to connect every pattern induced by the refined region to every pattern induced by the unrefined region. Such a complete set of rules is avaliable for simplices in the software-package $\mathcal{UG}$, see [10], where the 242 non-regular refinement rules has been automatically generated to prevent programming errors. Additionally, and also for non-simplex elements, it is possible to use a rule-set that will be computed at run-time, see [9, Chapter 6.9], and also guarantees the closure of the refined region in one element layer.

Note that generally using an incomplete set of rules, where regular refinement is used if the rules do not apply, may lead to unintended large refined regions.

IV. Local Multigrid Methods

The hierarchy of grids $\{\mathcal{T}_l\}_l$ and the edge element discretization on each level induce a hierarchy of linear systems of equations

$$\boldsymbol{A}_l \, \mathbf{x}_l = \mathbf{b}_l \qquad l = 0, \dots, L \, .$$

This hierarchy will be used by the multigrid method to solve the actual problem at level L efficiently with optimal amount of work, i.e. the computational work (time and memory) grows only linear in the number of unknowns N_L.

The main idea of multigrid is to use a classical iteration on each level (e.g. a Gauss-Seidel scheme) that can easily remove oscillatory error components and is therefore called a *smoother*, but cannot efficiently damp non-oscillatory error components. Then the problem is restricted to a coarser grid where it is solved resulting in a coarse grid correction that reduces the smooth error components. The idea can be applied recursively. For details, see [11].

The optimality of the multigrid method depends on two conditions:

1) The convergence rate is independent of the number of unknowns uniformly bounded away from one— roughly speaking the number of iterations will not grow for more unknowns.
2) The computational work for one iteration is $\mathcal{O}\big(N_L\big)$.

The second condition implies a geometrical growth of the number of unknowns,

$$N_l > q \, N_{l-1} \, , \qquad l = 1, \dots, L$$

for some $q > 1$, hence the amount of work for one multigrid iteration can be bounded by $\mathcal{O}\big(\frac{q}{q-1} N_L\big)$.

Using uniform refinement, this condition is easily met. However, in case of strongly locally refined grids, the condition can be violated. In the following subsections, we explain how condition two can be recovered even for these situations by using the concepts of local grids and vector classes.

A. The Active Set

Applying a multigrid sweep we think of a linear correction scheme defined by the matrix $\boldsymbol{B}_l$ of the form

$$\mathbf{x}_l^{i+1} = \mathbf{x}_l^i + \mathbf{c}_l^i \text{ with } \mathbf{c}_l^i = \boldsymbol{B}_l \mathbf{d}_l^i \text{ and } \mathbf{d}_l^i = \mathbf{b}_l - \boldsymbol{A}_l \, \mathbf{x}_l^i \, .$$

The underlying idea is to restrict the correction to an *active set* $\mathcal{A}_l$, which is defined by all degrees of freedom located at refined elements (i.e. red and green elements). Note that similar ideas go back to [12] and [13].

B. Vector Classes and Local Grids

In addition to the restriction of the multigrid correction to the active set, we require that the computation of the defect $\mathbf{d}_l$ and the smoothing can be performed on every level without communication to lower levels.

These goals can be achieved by local grids $\mathcal{T}_l^{loc} \subset \mathcal{T}_l$ which can be defined by introducing a vector class $\mathrm{class_l}(p) \in 0, 1, 2, 3$ for every degree of freedom $p \in \mathcal{P}_l$, where $\mathcal{P}_l$ is the set of all degree of freedoms on level l.

We define

$$\mathrm{class_l}(p) := \begin{cases} 3 \, , & \text{if } p \text{ is in the active set } \mathcal{A}_l \, , \\ 2 \, , & \text{if } \mathrm{class_l}(p) \neq 3 \text{ and there is a } T \in \mathcal{T}_l, \\ & \text{such that } p, q \in \mathcal{P}_l[T] \\ & \text{with } \mathrm{class_l}(q) = 3 \, , \\ 1 \, , & \text{if } \mathrm{class_l}(p) \neq 3, \mathrm{class_l}(p) \neq 2, \\ & \text{and there is a } T \in \mathcal{T}_l, \\ & \text{such that } p, q \in \mathcal{P}_l[T] \\ & \text{with } \mathrm{class_l}(q) = 2 \, , \\ 0 & \text{otherwise} \, , \end{cases}$$

where $\mathcal{P}_l[T]$ denotes the degree of freedoms at element T.

The vector class of a degree of freedom is its distance to the active set defined by the matrix graph. A correction of a degree of freedom p with $\mathrm{class_l}(p) = 3$ changes the defect for all p with $\mathrm{class_l}(p) \geq 2$. In order to compute these, the solution is necessary for p with $\mathrm{class_l}(p) \geq 1$.

The introduced vector classes directly leads to the definition of *a local grid at level l*,

$$\mathcal{T}_l^{loc} := \{T \in \mathcal{T}_l | \, \mathrm{class_l}(p) \geq 2 \text{ for at least one } p \in \mathcal{P}_l[T]\} \, .$$

Since at level 0 $\mathrm{class_0}(p) = 3$ for all $p \in \mathcal{P}_0$, it follows $\mathcal{T}_0^{loc} = \mathcal{T}_0$.

Only the local grids $\mathcal{T}_l^{loc}$—not the global $\mathcal{T}_l$—exist as objects in memory. This is important, because otherwise the memory requirement may not increase geometrically during the adaptive refinement, thus violating the second condition for the optimality of multigrid. Fig. 4 exhibits the difference between local and global grids by means of a 2D-grid hierarchy created by local refinement.

C. Hierarchical Consistency

We will write shortly $\mathbf{x}^{loc}$, $\boldsymbol{A}^{loc}$ for the restriction of vectors and matrices on the local grid. In order to compute the defect and the right hand side indeed on local grids, the correction- and the solution-vector, which are usually distributed over several levels, must be (hierarchically) *consistent*: A family of local vectors $\{\mathbf{x}_l^{loc}\}_{l=0,\dots,L}$ is called *hierarchically consistent*, if $\mathbf{x}_l^{loc}[p] = \mathbf{x}_{l-1}^{loc}[p] \quad \forall p \in \mathcal{P}_l$ with $\mathrm{class_l}(p) < 3 \, , \quad l = 1 \dots, L$. In the same manner, a family of local matrices $\{\boldsymbol{A}_l^{loc}\}_{l=0,\dots,L}$ is called *hierarchically consistent*, if $\boldsymbol{A}_l^{loc}[p,q] = \boldsymbol{A}_{l-1}^{loc}[p,q] \quad \forall p, q \in \mathcal{P}_l$ with $\mathrm{class_l}(p), \mathrm{class_l}(q) < 3 \, , \quad l = 1 \dots, L$.

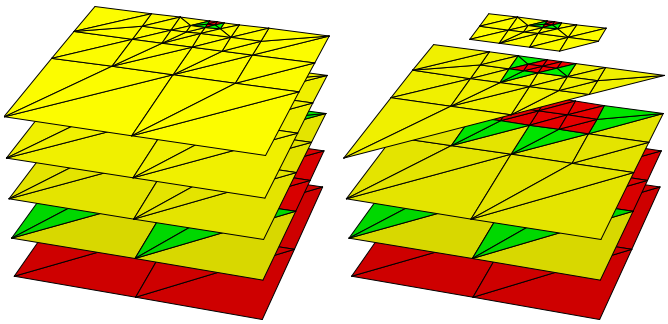

Fig. 4. 2D-hierarchy of global (left) and local (right) grids.

In contrast to the solution vector, the defect is not consistent, but can be reconstructed from the local defects recursively by

$$\mathbf{d}_l[p] = \begin{cases} \mathbf{d}_l^{loc}[p] & \text{if } \mathrm{class_l}(p) \geq 2 \\ \mathbf{d}_{l-1}^{loc}[p] & \text{otherwise} \end{cases}, \qquad l = 1, \ldots, L\,. \tag{8}$$

In the same way, the right hand side vector $\mathbf{b}$ is defined. Therefore, one has to take care that only $\mathbf{d}_l^{loc}[p]$ will be restricted with

$$p \in \mathcal{NDM}_l := \{q \in \mathcal{P}_l | q \notin \mathcal{P}_{l+1} \text{ or } \mathrm{class_{l+1}}(p) \geq 2\}\,,$$

$\mathcal{NDM}_l$ is called *new-defect-set*. Note that the prolongation of the correction does not need such a restriction.

D. Local Multigrid Cycle

Now we are in the position to write down the algorithm of a local multigrid cycle, where $\mathrm{S}_1^{loc}(\mathbf{c}_l^{loc}, \mathbf{d}_l^{loc})$ denotes the application of a local smoothing sweep, including an update of the defect, see Fig. 5.

procedure $\mathrm{MGC}^{loc}\,(l, \mathbf{c}_l^{loc}, \mathbf{d}_l^{loc})$
{
  if (l = 0) **then** solve $\boldsymbol{A}_0^{loc}\,\mathbf{c}_0^{loc} = \mathbf{d}_0^{loc}$
  else {
  {
    for $(1 \leq i \leq \nu_1)$ **do** $\mathrm{S}_1^{loc}(\mathbf{c}_l^{loc}, \mathbf{d}_l^{loc})$
    $\mathbf{d}_{l-1}^{loc}[p] \leftarrow \boldsymbol{r}_l^{loc}[p, \cdot]\,\mathbf{d}_l^{loc} \quad \forall p \in \mathcal{NDM}_{l-1}$
    $\mathbf{c}_{l-1}^{loc} \leftarrow 0$
    for $(1 \leq i \leq \gamma)$ **do** $\mathrm{MGC}\,(l-1, \mathbf{c}_{l-1}^{loc}, \mathbf{d}_{l-1}^{loc})$
    $\mathbf{w}_l^{loc} \leftarrow \boldsymbol{p}_l^{loc}\,\mathbf{c}_{l-1}^{loc}$
    $\mathbf{d}_l^{loc} \leftarrow \mathbf{d}_l^{loc} - \boldsymbol{A}_l^{loc}\,\mathbf{w}_l^{loc}$
    $\mathbf{c}_l^{loc} \leftarrow \mathbf{c}_l^{loc} + \mathbf{w}_l^{loc}$
    for $(1 \leq i \leq \nu_2)$ **do** $\mathrm{S}_2^{loc}(\mathbf{c}_l^{loc}, \mathbf{d}_l^{loc})$
  }
}

Fig. 5. Local multigrid cycle.

Finally, we note that for the smoothing of problems in $\mathbf{H}(\mathbf{curl}; \Omega)$, standard smoothing procedures will not work due to the large kernel of the curl operator. Special smoothers have been designed by Hiptmair [4] and Arnold Falk and Winther [14]. These smoothers need slightly enlarged local grids, see [1]. These enlarged local grids can be seen in some of the examples in the next section.

V. Numerical Examples

The described concepts and algortithms have been implemented in the adaptive finite element software $\mathsf{EM}_{\mathcal{UG}}$ (*electromagnetics on unstructured grids*), which is based on the simulation toolbox $\mathcal{UG}$, see [1], [10]. In this section $\mathsf{EM}_{\mathcal{UG}}$ will be used to compute several problems. We will start with some simple academic examples to study the basic behaviour, then we will move on to a TEAM benchmark problem. Finally, a realistic gas insulated switch-gear (GIS) will be computed.

A. Uniformly Refined Cube

In this example we study the iterative application of a V(1,1)-multigrid cycle using the Hiptmair-smoother with simple Gauss-Seidel sweeps.

The domain is the unit-cube $\Omega = (0, 1\,\mathrm{m})^3$ with Dirichlet boundary conditions $\mathbf{n} \times \mathbf{E} = 0$ and zero excitation. Consequently, zero is the solution of the problem. The initial grid, see Fig. 6, will be uniformly refined using the red-rule.

Here, we are interested in the asymptotic convergence speed which is defined by the maximum eigenvalue of the iteration matrix of the multigrid cycle. A good and computable approximation for this value is the *mean reduction-rate* or *measured convergence-rate*

$$\overline{\rho}_L^{(m)} := \left(\frac{\left\| \mathbf{d}_L^{(m)} \right\|}{\left\| \mathbf{d}_L^{(0)} \right\|} \right)^{\frac{1}{m}},$$

where $\mathbf{d}_L^{(m)}$ is the mth defect on level L.

The iterations have been started with a random solution vector $\mathbf{x}^{(0)}$. To minimize the dependence of the measured convergence-rate $\mathbf{d}_L^{(m)}$ on the initial solution $\mathbf{x}^{(0)}$

- the iteration is not terminated until the initial defect has been reduced by the large factor 10^{20} and
- the experiment is repeated several times and the mean value of the measured convergence rates will be taken as final value.

The resulting measured convergence rates are displayed in Tab. I for varying scaling $\beta := \omega\,\sigma/\nu$. Clearly, the convergence rates are practically uniformly bounded away from one and the scheme is robust in the relative scaling of the coefficients.

TABLE I
Convergence rates of the uniformly refined cube

β/m^{-2}	$L=1$	$L=2$	$L=3$	$L=4$	$L=5$
0.01	0.15	0.27	0.35	0.38	0.40
1.00	0.14	0.28	0.35	0.38	0.40
100.00	0.20	0.31	0.34	0.37	0.39

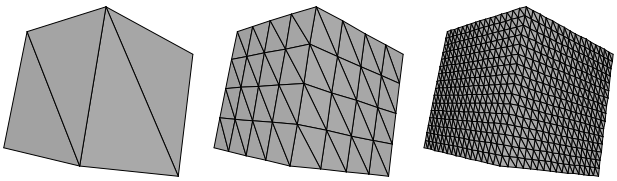

Fig. 6. Grid $\mathcal{T}_0$, $\mathcal{T}_2$ and $\mathcal{T}_4$ of the uniformly refined cube.

B. Locally Refined Cube

Now, we modify the previous experiment by starting with the uniformly refined grid hierarchy at level $L = 3$, but then we subsequently refine the cube at one corner *locally*, see Fig. 7. Note that the non-colored elements in Fig. 7 are not part of the local grids as described in Sec. IV and do not need any additional memory on the displayed grid level.

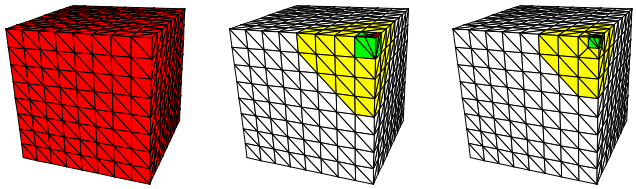

Fig. 7. Grid $\mathcal{T}_3$, $\mathcal{T}_4$, and $\mathcal{T}_5$ of the locally refined cube.

Table II shows the convergence rates applying the local multigrid method to this model problem. Comparing the convergence rates with the convergence rates of the uniformly refined cube in Tab. I, one can recognize a drop in the convergence rate from level 3 to level 4 for the locally refined cube. This can be explained by the lower mesh quality of the green closure that will be computed for the first time at level 4. During the following refinement the mesh-quality does not further detoriate because of the stability of the red-green-refinement. In addition, the convergence rates are still uniformly bounded away from one and are robust w.r.t. the relative scaling of the coefficients.

TABLE II

CONVERGENCE RATES OF THE LOCALLY REFINED CUBE

β/m^{-2}	$L=3$	$L=4$	$L=5$	$L=6$	$L=7$
0.01	0.35	0.43	0.42	0.41	0.41
1.00	0.35	0.44	0.40	0.40	0.40
100.00	0.34	0.43	0.41	0.41	0.41

C. Local Multigrid Pre-conditioner and Jumping Coefficients

The proposed local multigrid cycle can be used as a pre-conditioner, i.e. it can be accelerated by Krylov subspace methods like GMRES, BiCGStab [15] or TFQMR [16]. Here, we study the performance of a BiCGStab solver with local V(1,1)-multigrid pre-conditioner in case of jumping coefficients.

The computational domain is again the cube $\Omega = (0, 1\,\mathrm{m})^3$. The domain is subdivided into two disjoint subsets $\Omega_1 := (\frac{1}{3}\,\mathrm{m}, \frac{2}{3}\,\mathrm{m})^3$ and $\Omega_2 := \Omega \setminus \overline{\Omega_1}$. The initial triangulation is displayed in Fig. 8(a). It is constructed by 12 hexahedra, each divided into 6 tetrahedra. The initial triangulation has been locally refined with the aid of the error estimator, see Sec. III. In the refinement-strategy $\xi = 0.25$ has been used.

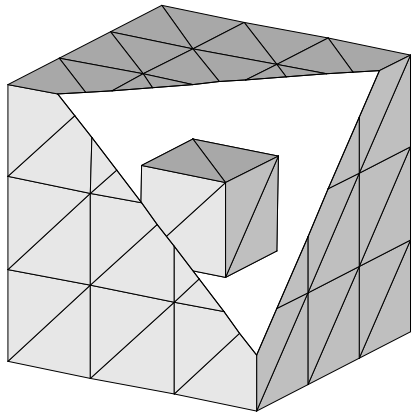

(a)

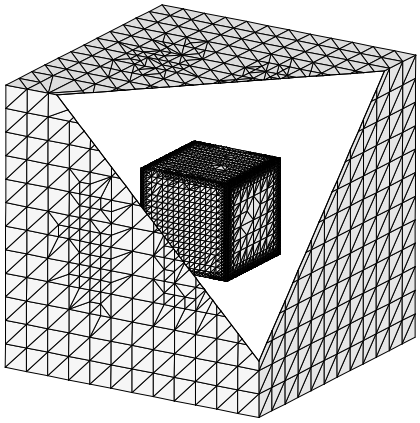

(b)

Fig. 8. Coarse grid $\mathcal{T}_0$ and $\mathcal{T}_6$ for the interior cube occupied by a highly permeable material (last line in Tab. III).

The coefficients are non-constant. We set

$$\nu(\mathbf{x}) := \begin{cases} \nu_1 & \text{if } \mathbf{x} \in \Omega_1\,, \\ 1 & \text{otherwise}\,, \end{cases} \quad \sigma(\mathbf{x}) := \begin{cases} \sigma_1 & \text{if } \mathbf{x} \in \Omega_1\,, \\ 1 & \text{otherwise} \end{cases}$$

and vary ν_1 and σ_1, while $\omega = 1\,\mathrm{s}^{-1}$. The initial solution is zero. The excitation is realized by inhomogeneous Dirichlet boundary conditions $\mathbf{n} \times \mathbf{E} = \mathbf{e}_z$ at the cube faces $x = const.$ and $y = const.$ At the other two faces homogenous Neumann boundary conditions $\mathbf{n} \times \nu\,\mathbf{curl}\,\mathbf{E} = 0$ are applied.

The number of BiCGStab-iterations using the local V(1,1)-multigrid pre-conditioner for a reduction of the defect by a factor of 10^{20} are shown in Tab. III, the associated number of unknowns for the finest meshes are shown in Tab. IV.

TABLE III
NUMBER OF ITERATIONS FOR JUMPING COEFFICIENTS USING LOCAL MG

ν_1	$\sigma_1/(\mathrm{S/m})$	L=1	L=2	L=3	L=4	L=5	L=6
1	1	22	27	26	28	–	–
1	10^4	26	25	29	35	37	36
1	10^{-4}	26	24	24	26	25	28
10^4	1	26	24	23	26	25	28
10^{-4}	1	26	27	31	37	38	39

TABLE IV
NUMBER OF UNKNOWNS ON THE FINEST MESH FOR JUMPING COEFFICIENTS USING LOCAL MG

ν_1	$\sigma_1/(\mathrm{S/m})$	$\max N_L$
1	1	1 438 398
1	10^4	522 210
1	10^{-4}	711 500
10^4	1	709 934
10^{-4}	1	590 678

A drop in the convergence speed can be observed if $\omega\sigma_1 \gg 1$ (highly conductive interior cube) or if $\nu_1 \ll 1$ (highly permeable interior cube). In both cases singularities at edges and corners of Ω_1 will arise, limiting the regularity of the solution. However, the number of iterations does not practically depend on the number of unknowns. The magnetic field and the final mesh for the second case is visualized in Fig. 9 and Fig. 8(b), respectively.

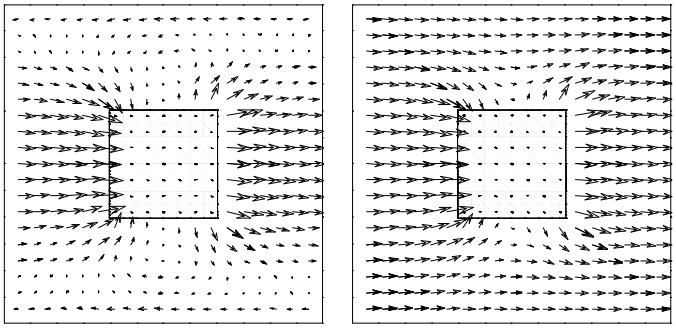

Fig. 9. $\mathrm{Re}\,\mathbf{H}$ (left) and $\mathrm{Im}\,\mathbf{H}$ (right) along a cut if the interior cube is occupied by a highly permeable material (last row in Tab. III), $L = 5$. There are singularities along the edges and corners of the interior cube.

D. TEAM 7 Benchmark Problem

To validate the proposed algorithms and their implementations for a more realistic situation, we consider the TEAM benchmark problem 7 (see [17]). The problem consists of an aluminum plate ($\sigma = 3.526\,10^7\,\mathrm{S/m}$) with a hole and an excitation coil above the plate with a time-harmonic driving current of $2742\,\mathrm{A}$. The driving current reaches the maximum

TABLE V
NUMBER OF ITERATIONS AND GRID SIZE OF THE TEAM7 BENCHMARK

	$L=0$	$L=1$	$L=2$	$L=3$	$L=4$	$L=5$
$N_{\mathcal{T}}$	$5.6\,10^3$	$4.5\,10^4$	$7.2\,10^4$	$8.0\,10^4$	$1.6\,10^5$	$3.8\,10^5$
$N_{\mathcal{E}}$	$6.7\,10^3$	$5.3\,10^4$	$8.8\,10^4$	$1.0\,10^5$	$2.0\,10^5$	$4.7\,10^5$
Iter	—	15	15	16	15	16

at $\omega t = 0$. The computational domain Ω was artificially restricted to a cube with $1\,\mathrm{m}$ edge length with boundary conditions $\mathbf{n} \times \mathbf{E} = 0$ on Γ.

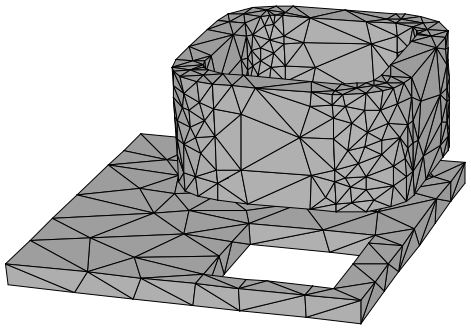

Fig. 10. Coarse grid $\mathcal{T}_0$ of the TEAM 7 benchmark problem. The grid of the surrounding air is not displayed.

To generate a hierarchy of grids we start with the base-level grid $\mathcal{T}_0$, see Fig. 10, and refine uniformly once yielding $\mathcal{T}_1$. The grid levels $l > 1$ are generated by adaptive local refinement using the residual error estimator. Grids up to level 5 are generated.

For the solution of the linear systems of equations, again, we apply BiCGStab with a local V(1,1)-MG-pre-conditioner with a Hiptmair-smoother.

In contrast to the previous examples, the TEAM 7 benchmark problem also consists of non-conductive regions (the complement of the aluminum plate). This means that using the singular formulation (5) the solution $\mathbf{E}$ is not unique in the non-conductive region, whereas the magnetic field is well defined. Thus, during a MG solution procedure, the L^2-norm of components in the kernel of the $\mathbf{curl}\,\mathbf{curl}$-operator can reach very large values, possibly leading to cancellation errors. To prevent this, an approximate orthogonal projection to the complement of the kernel is applied after each multigrid-sweep. This can be done at low costs by an additional multigrid-sweep on a Poisson problem. For more details, see [18].

Table V shows that the number of iterations remains constant during the refinement. Hence, the local multigrid pre-conditioner works very well for the benchmark problem.

The results at level 5 are displayed in Fig. 11–13 and exhibit good agreement with measured data.

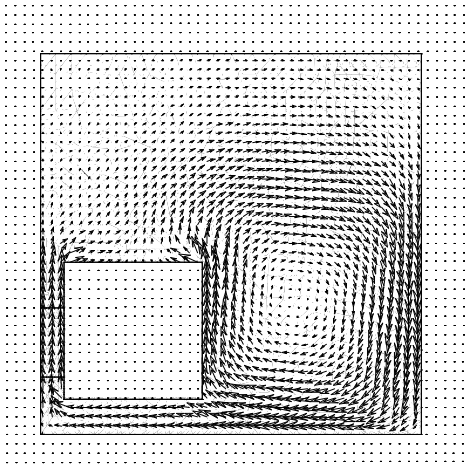

Fig. 11. $\mathrm{Re}\,\mathbf{J}$ in the plate of the TEAM 7 benchmark problem.

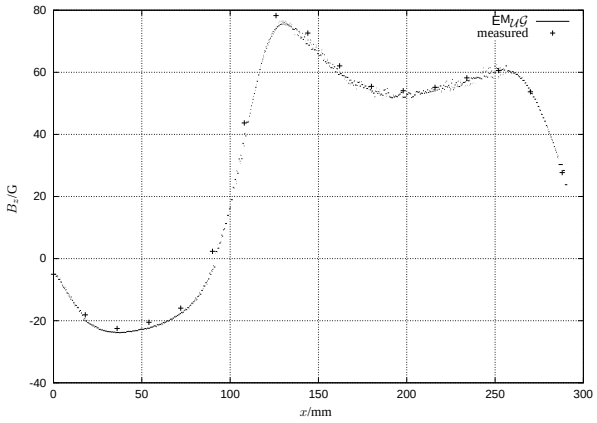

Fig. 12. Computed $\mathrm{sign}\,(\mathrm{Re}\,B_z)|B_z|$ along a pre-defined line of the TEAM 7 benchmark problem compared with measured values.

E. Gas Insulated Switchgear

The final example is a realistic model of a gas insulated switchgear (GIS). It mainly consists of an aluminum casing and three interior conductors, see Fig. 14(a). For simplicity the casing is assumed to be perfect conductive. This turns the original problem with an unbounded domain into an interior one with electric boundary conditions $\mathbf{n} \times \mathbf{E} = 0$.

The conductivity of the interior conductors is 26–$32 \cdot 10^6$ S/m, depending on temperature. For the simulation we take the mean value.

In contrast to the TEAM 7 benchmark problem, the currents in the conductive regions are not induced currents, but impressed currents. In each of the three conductors a time harmonic current of 4000 A at frequency 50 Hz is prescribed, with a phase shift of $\varphi = \frac{2\pi}{3}$ between each conductor current (three-phase current). The excitation is realized by thin current sources at the terminals on one side of the GIS.

For the solution we apply a local V(2,2)-multigrid solver with a symmetric Gauss-Seidel Hiptmair-smoother. In order to obtain some typical convergence rates for realistic complicated

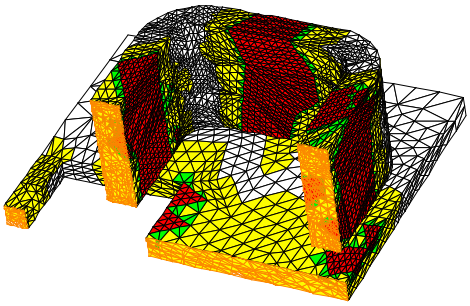

(a) local $\mathcal{T}_2$ with cut plane

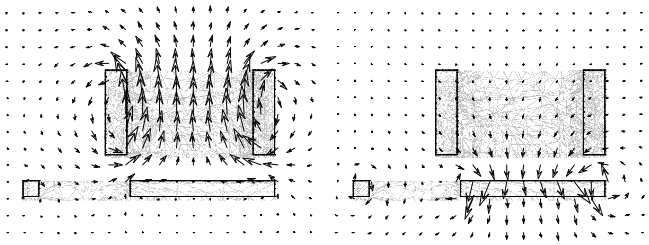

(b) $\mathrm{Re}\,\mathbf{H}$ at cut plane (c) $\mathrm{Im}\,\mathbf{H}$ at cut plane

Fig. 13. Local grid and magnetic field results of the TEAM 7 benchmark problem.

geometries, Krylov subspace acceleration is not used for this experiment.

The initial and the final grid after an adaptive computation are shown in Fig. 14. Due to the already large initial grid, there are only two levels of refinement. The resulting convergence rates and the mesh sizes are displayed in Tab. VI. The number of complex unknowns is 900k for the finest mesh.

TABLE VI
CONVERGENCE RATES AND MESH SIZES OF THE GIS-MODEL

	$L=0$	$L=1$	$L=2$
$N_{\mathcal{T}}$	$7.8\,10^4$	$6.3\,10^5$	$7.5\,10^5$
$N_{\mathcal{E}}$	$9.3\,10^4$	$7.4\,10^5$	$9.0\,10^5$
$\overline{\rho}_L^{(m)}$	—	0.58	0.59

It can be observed that the convergence rate is not as good as in the previous academic examples, although we used a V(2,2)-cycle in the GIS experiment, whereas in the academic examples we used only a V(1,1)-cycle-MG. The reason is that for complicated realistic problems it is much harder to generate initial meshes with high quality which has a strong influence on the MG convergence. Nevertheless, even for this realistic example, acceptable convergence rates are obtained, see Tab. VI.

In Fig. 15 the resulting magnetic field and the current density are displayed along cuts through the GIS geometry.

VI. Conclusion

The multigrid method has been used to solve large sparse complex symmetric linear equations arising from time harmonic eddy current modelling with finite elements based on a singular electric formulation.

The multigrid method features optimal complexity and is one of the fastest available solution strategies. However, the application of local adaptive mesh refinement may lead to a growth in the number of unknowns from one refinement level to next, that is too small to preserve the optimality of standard multigrid with global smoothing. It has been shown how this problem is overcome by a local multigrid method, that has been implemented by the concepts of local grids and vector classes. These concepts naturally

1) restrict the amount of memory to store locally refined grids and
2) localize the smoothing to the refined region at each level.

The investigation of several numerical examples has demontrated the validity of the presented local multigrid scheme and its implementation, even for realistic eddy current applications with very complicated geometry. Furthermore, it has been shown, that the presented local multigrid method works well with or without Krylov subspace acceleration.

Acknowledgment

The authors would like to thank Andreas Blaszczyk, ABB Corporate Research Center Baden-Dättwil, Switzerland, and ABB Calor Emag Hochspannung GmbH, Germany, for providing the gas insulated switchgear example.

References

[1] O. Sterz, "Modellierung und Numerik zeitharmonischer Wirbelstromprobleme in 3D," Ph.D. dissertation, Interdisziplinäres Zentrum für Wissenschaftliches Rechnen, Universität Heidelberg, 2003, (in German).

[2] A. Bossavit, "Two dual formulations of the 3-D eddy-currents problem," *COMPEL*, vol. 4, no. 2, pp. 103–116, 1985.

[3] ——, *Computational Electromagnetism. Variational Formulation, Complementarity, Edge Elements*, ser. Academic Press Electromagnetism Series. San Diego: Academic Press, 1998, no. 2.

[4] R. Hiptmair, "Multigrid method for Maxwell's equations," *SIAM J. Numer. Anal.*, vol. 36, no. 1, pp. 204–225, 1999.

[5] R. Beck, R. Hiptmair, R. Hoppe, and B. Wohlmuth, "Residual based a-posteriori error estimators for eddy current computation," $\mathrm{M^2AN}$, vol. 34, no. 1, pp. 159–182, 2000.

[6] R. Verfürth, *A review of a posteriori error estimation and adaptive mesh-refinement techniques*. Stuttgart: Teubner-Verlag, 1996.

[7] R. Bank, A. Sherman, and A. Weiser, "Refinement algorithm and data structures for regular local mesh refinement," in *Scientific Computing*, R. Stepleman et al., Ed., vol. 44. IMACS North–Holland, Amsterdam, 1983, pp. 3–17.

[8] J. Bey, *Finite-Volumen und Mehrgitterverfahren für elliptische Randwertprobleme*, ser. Advances in numerical mathematics. Stuttgart, Leipzig: Teubner, 1998, (in German).

[9] S. Lang, "Parallele Numerische Simulation instationärer Probleme mit adaptiven Methoden auf unstrukturierten Gittern," Ph.D. dissertation, Universität Stuttgart, Stuttgart, Germany, 2001, Mitteilungen des Instituts für Wasserbau, Heft 110 (in German).

[10] P. Bastian, K. Birken, K. Johannsen, S. Lang, N. Neuss, H. Rentz-Reichert, and C. Wieners, "UG—a flexible software toolbox for solving partial differential equations," *Computing and Visualization in Science*, vol. 1, pp. 27–40, 1997.

[11] W. Hackbusch, *Multi–grid Methods and Applications*. Springer–Verlag, Berlin, 1985.

[12] A. Brandt, "Multi-level adaptive solutions to boundary-value problems," *Math. Comp.*, vol. 31, no. 138, pp. 333–390, 1977.

[13] M. Rivara, "Design and data structure of a fully adaptive finite element software," *ACM Trans. Math. Software*, vol. 10, pp. 242–246, 1984.

[14] D. Arnold, R. Falk, and R. Winther, "Multigrid in $H(\mathrm{div})$ and $H(\mathbf{curl})$," *Numer. Math.*, vol. 85, no. 2, pp. 175–195, 2000.

[15] H. van der Vorst, "BI-CGSTAB: A fast and smoothly converging variant of BI-CG for the solution of nonsymmetric linear systems," *SIAM J. Sci. Stat. Comput.*, vol. 13, no. 2, pp. 631–644, 1992.

[16] R. Freund, "Transpose-free quasi-minimal residual methods for non-Hermitian linear systems," *IMA Volumes in Mathematics and its Applications*, vol. 60, no. 69, pp. 69–93, 1994.

[17] K. Fujiwara and T. Nakata, "Results for benchmark problem 7," *COMPEL*, vol. 9, no. 3, pp. 137–154, 1990.

[18] O. Sterz, "Multigrid for time harmonic eddy currrents without gauge," in *Scientific Computing in Electrical Engineering. Proceedings of the 4th International Workshop Scientific Computing in Electrical Engineering, Eindhoven, The Netherlands, June 23–28, 2002*, ser. *LNCSE*. Berlin: Springer, 2004.

[19] P. Bastian and G. Wittum, "On robust and adaptive multi–grid methods," in *Multigrid Methods IV, Proceedings of the Fourth European Multigrid Conference, Amsterdam, July 6-9, 1993*, ser. ISNM, vol. 116. Basel: Birkhäuser, 1994, pp. 1–17.

[20] C. Wieners, "The implementation of adaptive multigrid methods for finite elements," Universität Stuttgart, Germany, SFB 404 Preprint 97/12, 1997.

[21] ——, "Local multigrid methods on hierarchical meshes," in *Proceedings of the 17th GAMM-Seminar*, Leipzig, 2001, pp. 1–8.

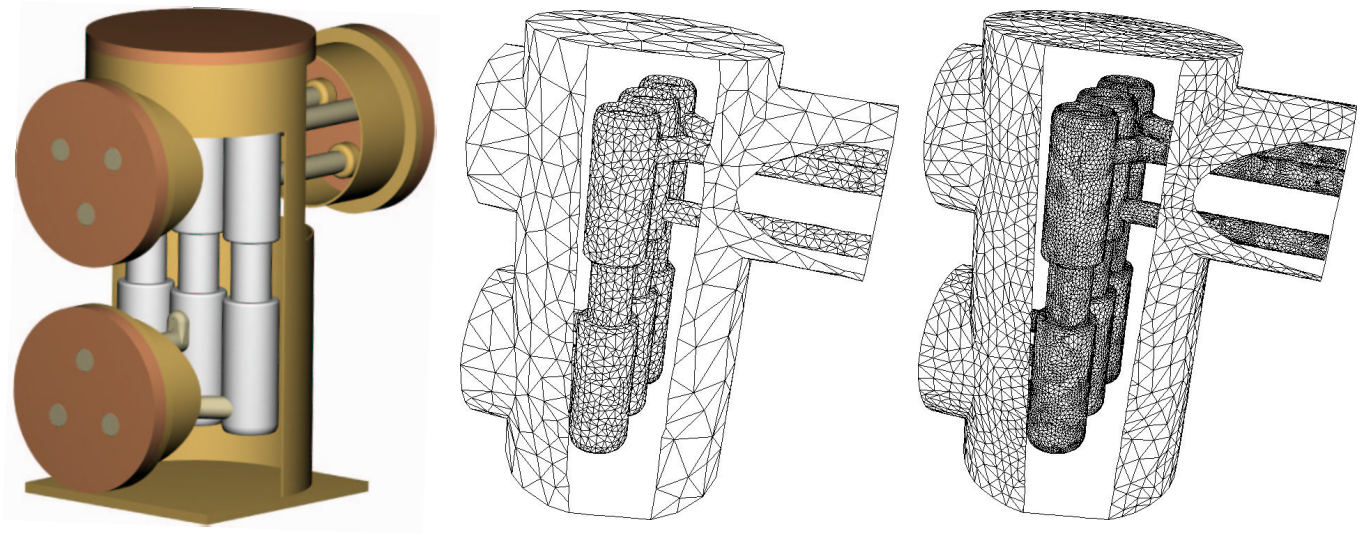

(a) CAD model (b) Grid $\mathcal{T}_0$ (c) Grid $\mathcal{T}_2$

Fig. 14. CAD geometry of the GIS model, grids on level 0 and 2.

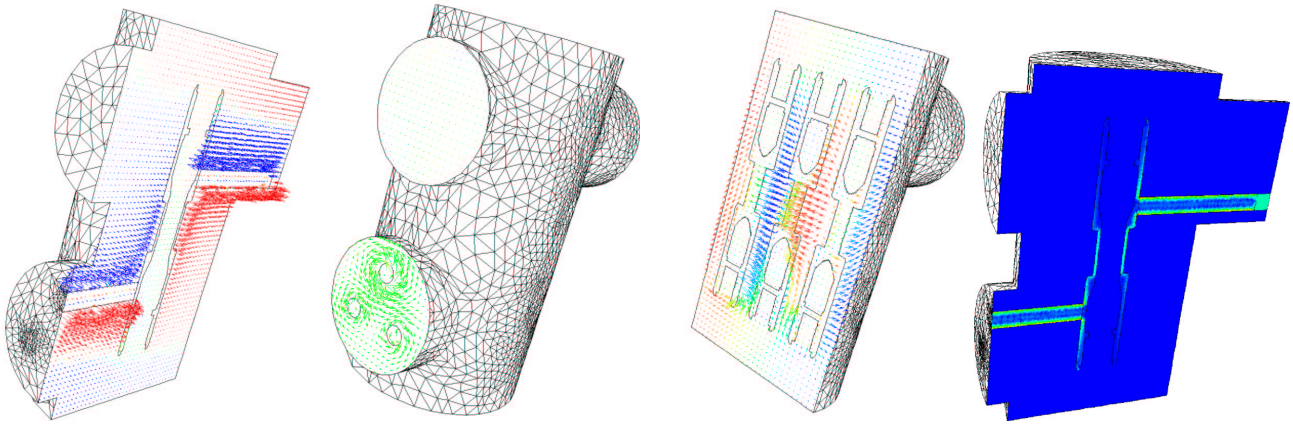

(a) $\mathrm{Re}\,\mathbf{H}$ (b) $\mathrm{Re}\,\mathbf{H}$ (c) $\mathrm{Re}\,\mathbf{H}$ (d) $|\mathrm{Re}\,\mathbf{J}|$

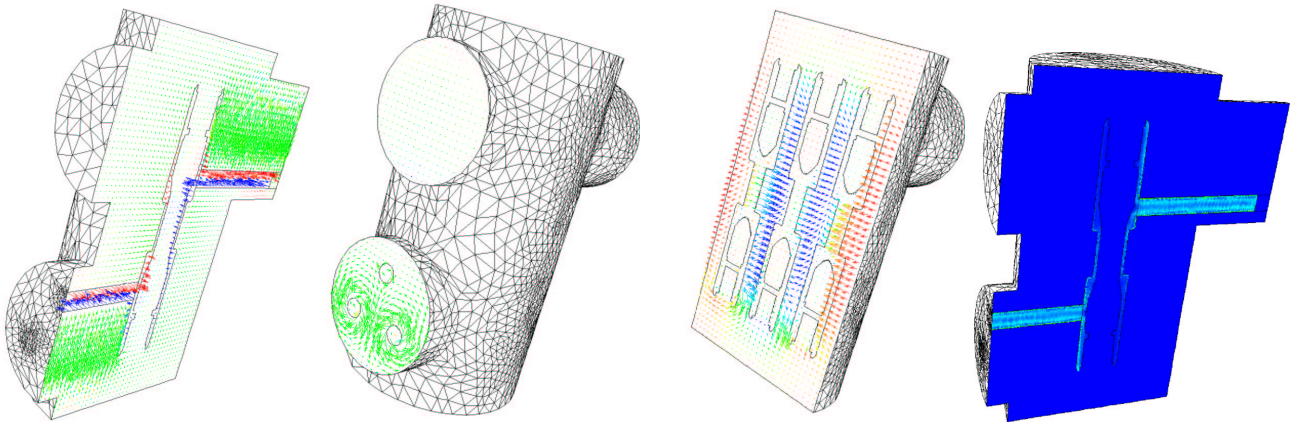

(e) $\mathrm{Im}\,\mathbf{H}$ (f) $\mathrm{Im}\,\mathbf{H}$ (g) $\mathrm{Im}\,\mathbf{H}$ (h) $|\mathrm{Im}\,\mathbf{J}|$

Fig. 15. Result-plots for the GIS model at $\omega t = 0$ and $\omega t = \frac{3\pi}{2}$ at cuts.